DFT-Based Study for the Enhancement of CO_2 Adsorption on Metal-Doped Nitrogen-Enriched Polytriazines

Hieu Minh Ngo, Umapada Pal, Young Soo Kang,* and Kang Min Ok*

Cite This: *ACS Omega* 2023, 8, 8876−8884

Read Online

ACCESS | Metrics & More | Article Recommendations | Supporting Information

ABSTRACT: Nitrogen-enriched polytriazine (NPT), a carbon nitride-based material, has received much attention for CO_2 storage applications. However, to enhance the CO_2 uptake capacity more efficiently, it is necessary to understand the interaction mechanism between CO_2 molecules and NPT through appropriate modification of the structures. Here, we introduce a method to enhance the CO_2 adsorption capacity of NPT by incorporating metal atoms such as Sn, Co, and Ni into the polytriazine network. DFT calculations were used to investigate the CO_2 adsorption mechanism of the polytriazine frameworks by tracking the interactions between CO_2 and the various interaction sites of NPT. By optimizing the geometry of the pure and metal-containing NPT frameworks, we calculated the binding energy of metal atoms in the NPT framework, the adsorption energy of CO_2 molecules, and the charge transfer between CO_2 molecules and the corresponding adsorption systems. In this work, we demonstrate that the CO_2 adsorption capacity of NPT can be greatly enhanced by doping transition-metal atoms into the cavities of NPT.
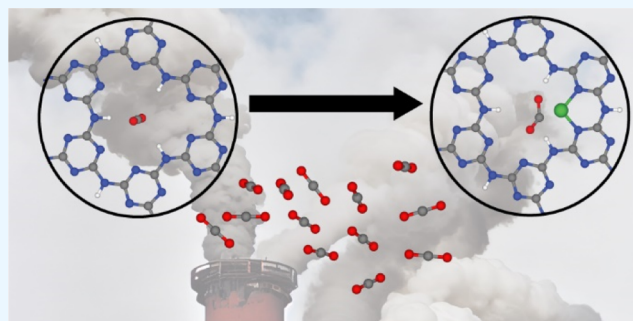
INTRODUCTION

CO_2 emissions from human activities have become a significant contributor to global warming and its associated consequences, including climate change, rising sea levels, and acid rain.[1] To address this crisis, the development of cost-effective materials that can efficiently capture CO_2 is crucial.[2,3] Solid-state materials, such as zeolites,[4] metal−organic frameworks,[5] mesoporous silica,[6] and carbon-based adsorbents[7] have been studied for their potential to capture CO_2 due to their high adsorption capacity, stable structure, high porosity, large total pore volume, and high specific surface area. Recently, researchers have been turning their attention to two-dimensional (2D) materials such as molybdenum disulfides,[8] graphynes,[9] covalent organic frameworks,[10] borophenes,[11] and carbon nitrides.[12] These materials have attracted attention due to their exceptional mechanical and thermal properties, tunable band structures, and ultrahigh specific surface areas,[13] which make them potential CO_2 capture candidates. In fact, recent studies reveal that graphenes[14] and carbon nitrides[15] have remarkable CO_2 capture capacities. To further understand the mechanisms involved, researchers have used density functional theory (DFT) calculations and predicted the adsorption of CO_2 on various 2D materials such as BC_3 nanosheets,[16] graphynes,[17] and graphenes.[18] In this manuscript, we present a DFT study of CO_2 adsorption on polytriazine structures, adding to a growing body of research on the use of 2D materials for CO_2 capture.

Within the carbon nitride family, polytriazine networks have been identified as having high surface area, high nitrogen content, and active sites that make them promising candidates for next-generation CO_2 capture.[12,19,20] The presence of amine functional groups, which can weakly adsorb CO_2 through acid−base interactions,[21] in combination with the high specific surface area of these materials, further enhance their potential.[15,22] The introduction of point defects and metal doping can also create more exposed active sites and improve the performance of these materials.[19,23−27]

Despite the potential of carbon nitride-based materials for CO_2 capture, the mechanisms behind CO_2 adsorption in metal- and nitrogen-doped porous carbonaceous structures, particularly in polytriazine networks, are not yet fully understood. In this study, we address this gap in knowledge by using density functional theory calculations to investigate the effect of single metal atoms such as Sn, Co, and Ni on the CO_2 capture capacity of polytriazine networks. These metals are selected because of their high reactivity, stability, and affinity for CO_2, which play an important role in improving the CO_2 adsorption capacity and overall efficiency and improving the gas adsorption properties of carbonaceous materials.[25,28−34]
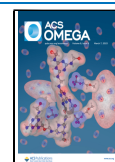
COMPUTATIONAL DETAILS

The projector augmented wave[35] approach was used to carry out all of the periodic DFT calculations[36,37] using the Vienna ab initio simulation package (VASP).[38,39] The generalized gradient approximation (GGA), applying Perdew−Burke−Ernzerhof as correlational functional,[40] was used as the exchange−correlation potential. We used the DFT-D3 dispersion correction method[41] to represent the van der Waals interactions for molecular adsorption on the surface to improve the accuracy of CO_2 adsorption energy calculations. The results were further processed using the VASPKIT[42] and VESTA[43] programs. The structures were fully relaxed until the magnitude of the Hellmann−Feynman force was less than 0.01 eV·Å^{-1}, and the convergence threshold for self-consistent field calculations was set to 10^{-5} eV per cell.

The pristine NPT and metal-doped NPT structures were considered, in which we treated the metal atoms as interstitial defects of the NPT system. The CO_2−NPT system was simulated using the slab method, by adding a vacuum region in the direction perpendicular to the NPT sheet of at least 15 Å, to eliminate interactions between the periodic images. The Kohn−Sham orbitals were expanded in a plane wave basis set with an energy cutoff of 520 eV. For optimizing the geometrical structure of the conventional NPT unit cell, a Γ-centered 4 × 4 × 4 k-point mesh of the first Brillouin zone was used. For the single layers and the adsorption systems, a (2 × 2) supercell and a Γ-centered 2 × 2 × 1 k-point mesh were utilized. For the systems containing transition-metal atoms such as Ni and Co, the spin polarization was appropriately included. The spin polarization was not included in the system with only Sn and other elements (C, N, O, and H) because there are no unpaired electrons in these atoms or molecules.[44]

An isolated CO_2 molecule was modeled as a single molecule at the center of a vacuum box with the size of 30 Å using the Γ k-point. The other settings were made as described above. By carefully moving up the accuracy ladder, a structural optimization was carried out to find the most stable geometries for the adsorption system, CO_2−NPT. The adsorption energy, charge transfer quantity, and change in work function for the most energetically stable configurations were then calculated. After considering pristine and metal atom-doped NPT structures, the binding energy of the metal atom was calculated by using the following equation[45−48]

$$E_b = E_{M/NPT} - E_{NPT} - E_M \qquad (1)$$

where E_b, $E_{M/NPT}$, E_{NPT}, and E_M are the binding energy, the total energy of the doped system, the total energy of the NPT, and the chemical potential of metal atoms, respectively. We considered the total energies of isolated Ni, Co, and Sn atoms as corresponding E_M (M = Ni, Co, or Sn).

The CO_2 adsorption energy (E_{ads}) on the NPT surface is defined by[11,49]

$$E_{ads} = E_{tot} - (E_{CO_2} + E_{NPT}) \qquad (2)$$

where E_{tot} is the total energy of the final system (CO_2−NPT), E_{CO_2} is the total energy of an isolated CO_2 molecule in the gas phase, and E_{NPT} is the total energy of the isolated NPT system. We used the Bader charge analysis code created by the Henkelman group[50] to determine the amount of charge transfer from NPT to CO_2. The work function was defined as $\phi = E_{vac} - E_F$, where E_{vac} and E_F are the vacuum level and the Fermi energy, respectively.

Molecular orbital projected density of states (MOPDOS) of CO_2 adsorbed on the substrate was performed using the MOPDOS from the VASP package.[51] To understand the interaction between the CO_2 and NPT substrates better, we conducted crystal orbital Hamilton population (COHP) analysis using the Local-Orbital Basis Suite Towards Electronic-Structure Reconstruction (LOBSTER)[52,53] and Lobster-Py packages,[54] installed with the Python Materials Genomics (Pymatgen, an open-source Python library)[55] and ChemEnv.[56] The basis set pbeVASPfit 2015 in LOBSTER was used.[57,58] The COHP was analyzed by using the wxDragon visualization program.[59] The vibrational frequencies of CO_2 molecules were calculated using harmonic approximation and finite difference approximation by diagonalizing the mass-weighted Hessian matrix.

RESULTS AND DISCUSSION

Optimized Structure of Pristine Monolayer NPT. We applied periodic boundary conditions[60] to represent the single-layer NPT polymer structure precisely. The NPT structure was modified from the known structure of intercalated polytriazine,[61] by removing intercalated Li and Cl ions and adding H into the N bridging. After that, the bulk crystal structure of pristine NPT was optimized as described in the Computational Details section. The calculated unit cell parameters were optimized to be ca. a = 8.60 Å, b = 8.60 Å, c = 7.00 Å, α = 90.0°, β = 90.0°, and γ = 120.0°. The results are in good agreement with the previous calculations and experiments.[61−66]

The monolayer NPT was created by slicing the bulk crystal structure of NPT along the (001) plane. A 2 × 2 × 1 NPT supercell consisting of 36 N atoms, 24 C atoms, and 12 H atoms was used in this study. To prevent recurrent interactions with nearby slabs, the interlayer distance was adjusted to 15 Å along the z-direction. The slab model of the monolayer NPT was optimized using the Computational Details provided in Section 2. As can be seen in Figure 1, the 2 × 2 × 1 NPT single-layer
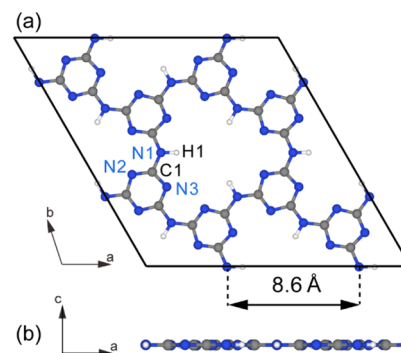

Figure 1. (a) Top view and (b) side view of the optimized structure for 2 × 2 × 1 NPT single-layer supercell (dark gray, C; blue, N; white, H).

supercell is a hexagonal structure with six triazine rings (C_3N_3) that are connected by NH bridging groups, in which the optimized lattice constant is ca. 8.60 Å. The calculated bond lengths of C1−N1, C1−N2, C1−N3, and N1−H1 are 1.37, 1.33, 1.35, and 1.01 Å, respectively. The optimized structure of monolayer pristine NPT revealed a stable planar configuration, as shown in Figure 1.

Geometric Structures of a Single Metal Atom Confined in the NPT Monolayer. Because of the hollow hexagonal structure, the NPT has a variety of high-symmetry

adsorption sites, resulting in the site discrimination in the electronic state (Figures 1 and S1). Seven possible adsorption sites around the sixfold cavity of the $2 \times 2 \times 1$ NPT supercell were considered in order to determine the most advantageous adsorption configuration for a single metal atom containing a pure NPT structure (Figure S1). While site 1 is at the center of the hollow space or cage of the NPT network, site 2 is at the hollow space near the two closely located nitrogen atoms of the triazine rings. Site 3 is close to the NH group, whereas site 4 is on the NH group. Sites 5, 6, and 7 are on the N atom, C atom, and at the center of the triazine ring, respectively. The detailed site positions for single metal atom species are presented in Figure S1. Once the structure was optimized, site 2 was found to be the most favorable adsorption position for all three metal atoms (Sn, Co, and Ni) because the system revealed the lowest energy. Therefore, we selected the site 2 for investigating doping effects further. The doped metal atoms were then treated as interstitial defects in the system. The fully relaxed, optimized structures of the metal-doped NPT systems are shown in Figure 2. Among the
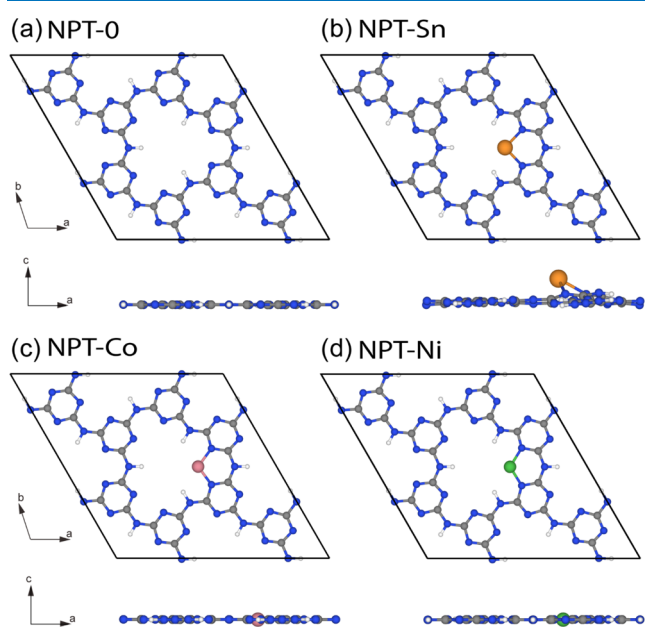
Figure 2. Structures of optimized $2 \times 2 \times 1$ single layer supercells in the *ab*-(top view) and *ac*-planes (side view) for (a) pristine NPT, (b) NPT-Sn, (c) NPT-Co, and (d) NPT-Ni (dark gray, C; blue, N; white, H; orange, Sn; magenta, Co; and green, Ni).

three metal atoms, transition metals, Ni and Co are seen to be more favorably doped and form planar features with NPT, whereas the post-transition metal, Sn atom is less likely to be incorporated into the NPT structure and stay above the planar geometry (Figure 2). The binding energies of single Sn, Co, and Ni atoms were estimated to be about −1.48, −1.95, and −2.20 eV, respectively (Table 1). More negative value of binding

Table 1. Binding Energy (E_b, eV) and the Difference between Binding Energy and Cohesive Energy ($|E_c − E_b|$, eV) for Three Metal Atoms at the Hollow Site of NPT Structure[a]

doped metal	Sn	Co	Ni
E_b	−1.48	−1.95	−2.20
$|E_c − E_b|$	1.66	2.44	2.24

[a]The cohesive values were taken from ref 72.

energy indicates a more energetically favorable interaction between the metal atoms and the NPT network. These results show that positions at the hollow sites of the sixfold cavity, near N atoms of triazine rings, are energetically favorable for Co, Ni, and Sn single atoms to be doped into the NPT structure. Similar results were also observed for other metal atoms in the polytriazine system[67] and carbon nitride-based systems.[68−70] Note that the binding energy of Sn is the least negative among the three metals. In addition, the out-of-plane position of Sn suggests that the Sn atom is weakly bound to the NPT system in comparison to the in-plane positions of Co and Ni. The results are consistent with the average bond lengths between the doped metal atoms and the two nearest N atoms. As can be seen in Table S1, while the bond lengths of Ni−N (1.79 Å) and Co−N (1.82 Å) are quite similar, that of Sn−N (2.28 Å) is the longest among the three metals. The bonding nature of metal atoms with their two adjacent atoms is presented by the ICOBI values and the Loewdin charges (Tables S1 and S3).[71] The ICOBI values of Sn−N (0.57), Co−N (0.48), and Ni−N (0.42), along with the Loewdin charge, indicate that the bonds between metal atoms and an adjacent nitrogen atom are coordination bonds, that is, a mixture of ionic and covalent bonds. The Sn−N bond reveals the highest covalent character among the three reported metal-doped NPT systems.

By analyzing the binding energy (E_b) and the cohesive energy (E_c) of individual atoms, we can gain a deeper understanding of the fundamental interactions and mechanisms involved in the growth process, as well as the specific properties and behaviors of individual metal atoms when interacting with the NPT network. This understanding is also useful in identifying potential issues and challenges that may arise during the growth process of metal atoms, such as the formation of impurities or defects. The experimental cohesive energy per atom for bulk Sn, Co, and Ni is −3.14, −4.39, and −4.44 eV/atom, respectively, which is significantly higher than the binding energies of these metals toward the NPT system (Table 1).[72] This implies that there is a possibility of metal clustering rather than implementing metal atom decoration.[73] However, a larger value of $|E_c − E_b|$ indicates that high thermal energy is required to make cluster aggregation, while a smaller value of $|E_c − E_b|$ indicates that the impurity island agglomeration is easier.[74] Of the three reported metals, Sn, with the smallest value of $|E_c − E_b|$, is most likely to agglomerate into clusters. However, since the current study only considers the case of single-atom doping in NPT, the possibility of metal cluster formation or 3D growth is not further discussed.

Electronic Structures of Single Metal Atom (Ni, Co, or Sn)-Doped NPT Monolayer. The densities of states for pristine NPT and metal-doped NPT (NPT-Sn, NPT-Co, and NPT-Ni) are presented in Figure 3. The calculated gaps between the highest occupied molecular orbital (HOMO) and the lowest unoccupied molecular orbital (LUMO) of the pristine NPT, NPT-Co, NPT-Ni, and NPT-Sn are 3.20, 0.65, 0.65, and 0.36 eV, respectively. As can be noticed, once the metal atoms are incorporated into the NPT framework, the HOMO−LUMO gap decreases significantly. In addition, the work functions of the pristine NPT, NPT-Co, NPT-Ni, and NPT-Sn are calculated to be of 5.51, 3.21, 3.21, and 3.36 eV, respectively (Table 2). Both the VB and CB of pristine NPT predominantly consist of N and C atom orbitals (Figure 3a). Upon introducing the single metal atom into the NPT monolayer, the DOSs of metal-doped NPTs change significantly (Figures 3 and S2). Incorporation of metal atoms into the NPT framework shifts the valence band to higher
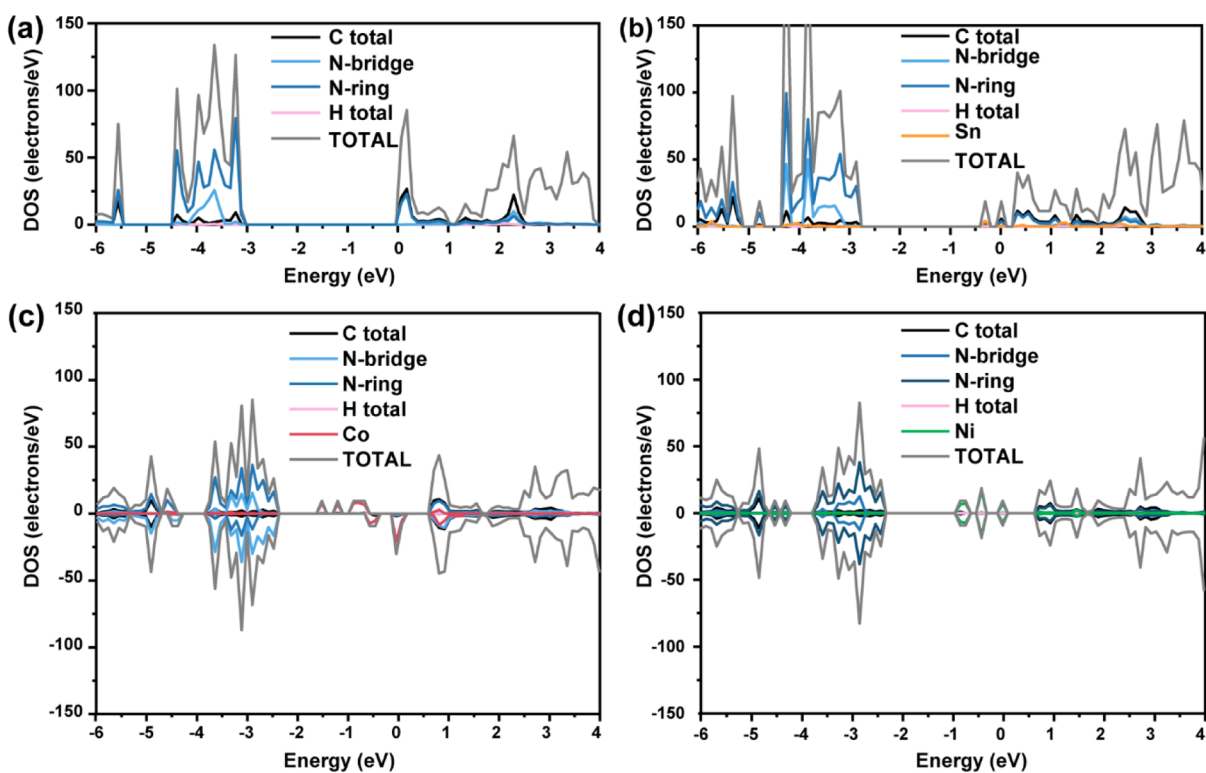
Figure 3. Density of states for (a) pristine NPT, (b) NPT-Sn, (c) NPT-Co, and (d) NPT-Ni. Fermi energy is set to 0.

Table 2. Work Function of Pristine and Metal Atom-Doped NPT Systems

	NPT-0	NPT-Co	NPT-Ni	NPT-Sn
Φ (eV)	5.51	3.21	3.21	3.36

energies and creates new dopant states between −2 and 2 eV. It should be noted that these new dopant states form both above and below the Fermi level, which results in a reduction of the band gap. Therefore, the HOMO−LUMO gaps of the metal-doped NPTs decrease significantly, effectively enhancing the photoresponse of the organic frameworks toward visible light. Figures 3 and S2 reveal that the new defect states formed due to metal atom incorporation readily donate electrons to states just below the Fermi level and readily accept electrons from states above the Fermi level. Therefore, the metal doping sites can play important roles in the electron transfer from the adsorbate to the substrate and vice versa. The corresponding HOMO and LUMO of NPT systems are presented in Figure 4. As illustrated in Figure 4a, while the orbital lobes for the HOMO are formed on all the atoms across the layers, those for the LUMO are only localized on the triazine ring, in which the NH groups act as charge-transporting bridges. The HOMOs for the metal-doped NPT systems are formed in the regions around the metals, whereas the LUMOs are delocalized in all of the atoms except for the NH bridging groups. Thus, metal atoms may exhibit oxidation activities in photocatalytic reactions.[69,75]

Interaction of CO_2 with Pristine NPT and Metal-Doped NPT Structure. We investigated the adsorption of CO_2 molecules on pristine and metal-doped NPT structures, considering seven possible CO_2 adsorption sites (Figure S1). The center of the hollow site (site 1) was found to be the most energetically favorable for CO_2 adsorption. Further analysis was conducted on this site, and the optimized structures for
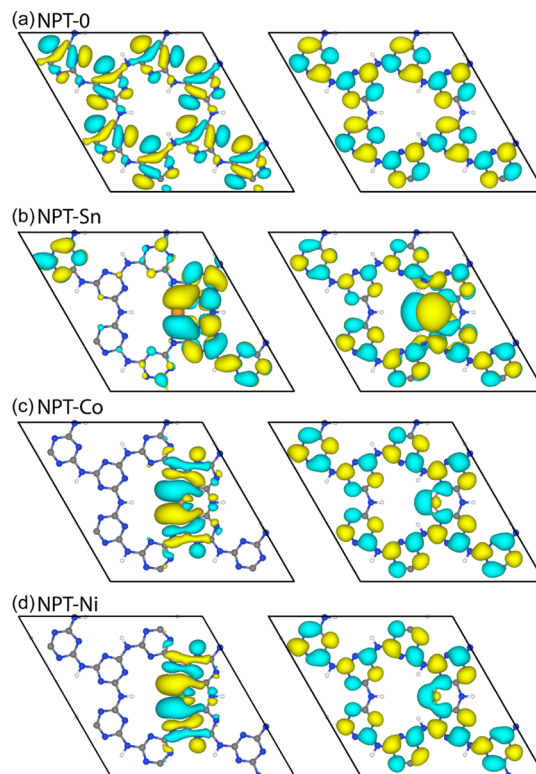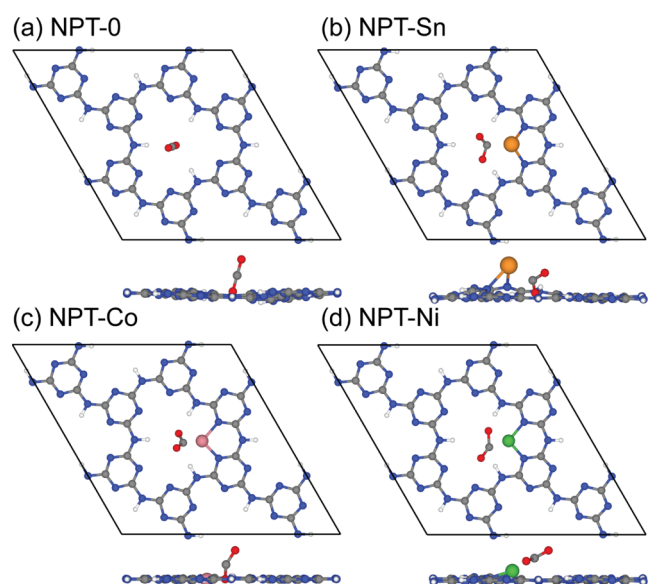

Figure 4. HOMO (left) and LUMO (right) of (a) pristine NPT, (b) NPT-Sn, (c) NPT-Co, and (d) NPT-Ni (dark gray, C; blue, N; white, H; orange, Sn; magenta, Co; and green, Ni).

adsorbed CO_2 on each system are shown in Figure 5. The adsorption energies of CO_2 on NPT-0, NPT-Sn, NPT-Ni, and NPT-Co systems were estimated to be −0.26, −0.69, −1.90, and

Figure 5. Top and side views of the optimized structures for CO_2 molecules adsorbed on the $2 \times 2 \times 1$ single layer supercells of (a) pristine NPT, (b) NPT-Sn, (c) NPT-Co, and (d) NPT-Ni (dark gray, C; blue, N; red, O; white, H; orange, Sn; magenta, Co; and green, Ni).

Figure 6. Charge density difference of CO_2 adsorbed on (a) NPT-0, (b) NPT-Sn, (c) NPT-Co, and (d) NPT-Ni.

−1.76 eV, respectively. The negative sign in the energy values indicates an exothermic interaction between the CO_2 molecule and the NPT structure. The interaction between the adsorbate and the adsorbent is minimum in the case of physisorption. However, in the case of chemisorption, there is a strong interaction that can result in a deformation of the adsorbate's geometry, which can greatly perturb the electronic structure of the NPT systems. The bending geometry of CO_2 molecules in the NPT-Co, NPT-Ni, and NPT-Sn systems clearly shows chemisorption, despite the weaker binding energy of CO_2 to the NPT-Sn system (−0.69 eV).

The Bader charge analysis (Table 2) showed that CO_2 is an electron donor for NPT-0, but the presence of metal atoms can change the electronic properties of CO_2 and its role from electron donor to electron acceptor. This change is reflected in the optimized structure of NPT-0, where the adsorbed CO_2 has a linear geometry (Figure 5), and in the metal-doped systems, where CO_2 becomes more anionic, adheres to the substrate in a nonlinear manner. The work function of NPT-0 remains unchanged by CO_2 adsorption. However, the work functions of NPT-Sn, NPT-Ni, and NPT-Co increase by +1.27, +0.69, and +0.64 eV, respectively, due to the donation of charge by metal atoms to CO_2 molecules, increasing the overall potential barrier. The charge density differences of CO_2 on different substrates are shown in Figure 6, with red indicating an electron-deficient state and blue indicating electron accumulation. The results are consistent with the Bader charge analysis, which predicts that the metal atoms donate electrons to CO_2, making it anionic and causing a bending of the O═C═O bond.[76] The calculated vibrational frequencies of CO_2 are presented in Table S5 and Figure S6. As can be seen in Table S5, all the molecular vibrations of CO_2 are affected by its adsorption on the NPT network. While the frequency of in-plane bending increases upon adsorption, the frequency of all other vibrations reduced after adsorption on NPT network; significantly on NPT doped metal systems.

A comparison of the DOS of free CO_2 and CO_2 molecules adsorbed on NPT systems is presented in Figure 7. The COHP
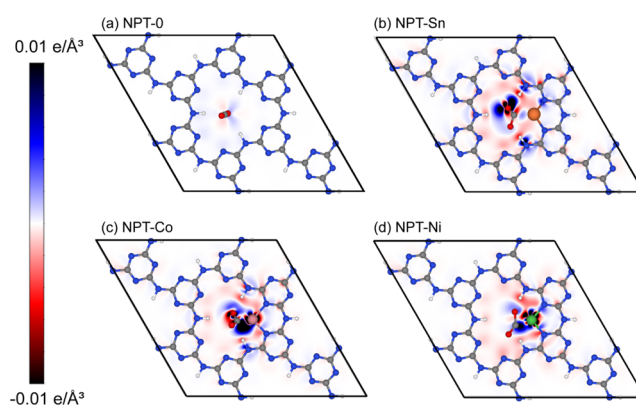
analysis in Figure 8 reveals the interactions between the carbon and oxygen atoms in a free CO_2 molecule and CO_2 molecules adsorbed on NPT-0, NPT-Sn, NPT-Co, and NPT-Ni. By comparing the energies and bandwidths of the same molecular orbitals (MOs) in an isolated CO_2 molecule (left), one can trace the interactions of the CO_2−NPT system.[77] The total DOS of CO_2 has eight peaks, each corresponding to one of the eight MO energy levels. The three MOs appearing in 7−10 eV are antibonding states, corresponding to σ_u*, π_u*, and ($\sigma_u* \sigma_g*$), respectively. The MOs near 0 and −5 eV are nonbonding states, corresponding to ($\pi_g \pi_u$) and σ_g, respectively, whereas those at −4 eV correspond to $\sigma_g \sigma_u \pi_u$. Two peaks near −20 and −22 eV are bonding states, corresponding to π_u and π_g MO energy levels, respectively (Figure S3).[78] Once the CO_2 is adsorbed on NPT-0, the energy of all MOs energy states reduces, indicating an enhancement of C−O bonding energy. However, after adsorption of CO_2 on the metal-doped NPT substrates, the HOMO−LUMO gap of CO_2 reduces significantly.

The interaction between the metal atoms and CO_2 molecule was studied by comparing the orbital contributions of metal atoms in NPT-doped systems and the molecular orbitals (MOs) of isolated CO_2 (Figure S5). The density of states (DOS) and crystal orbital Hamilton populations (COHP) analysis reveal strong interactions between metal atoms and CO_2 (Figures 7, 8, S2, S3, and S5). Despite the change in energy, the two MOs of CO_2 (π_u, π_g) near −20 eV remained localized after adsorption. The other MOs of CO_2 became delocalized. In the case of NPT-Ni, NPT-Co, and NPT-Sn, the three antibonding MOs of CO_2 mixed with Ni 4s, Co 4s, and Sn 5p orbitals and became spread out toward lower energies. The nonbonding MOs ($\pi_g \pi_u$) of CO_2 hybridize with Ni d, Co d, and Sn 5p orbitals. The two bonding MOs ($\sigma_g \sigma_u \pi_u$ and σ_g) of CO_2 interact with Ni dπ (xy, yz), Co dπ (xy, yz), and Sn 5s orbitals and become delocalized.

Table S4 provides additional information about the interaction of the CO_2 molecule with metal atoms, including the bond distances, ionic crystal orbital Hamilton populations (ICOHP), and ionic crystal orbital bond index (ICOBI). The ICOHP values indicate bond strength,[79] while the ICOBI values indicate chemical bond order based on covalency.[53] The low ICOBI values and Loewdin charges from interactions between metal atoms and O of CO_2 suggest that the interactions tend to have an ionic character. The larger ICOBI values from interactions between metal atoms and C indicate a more covalent character. The highest ICOBI value of 0.80 from the interaction between Sn and C represents a strong covalent bond. Upon adsorption of CO_2, the ICOHP values for bonding
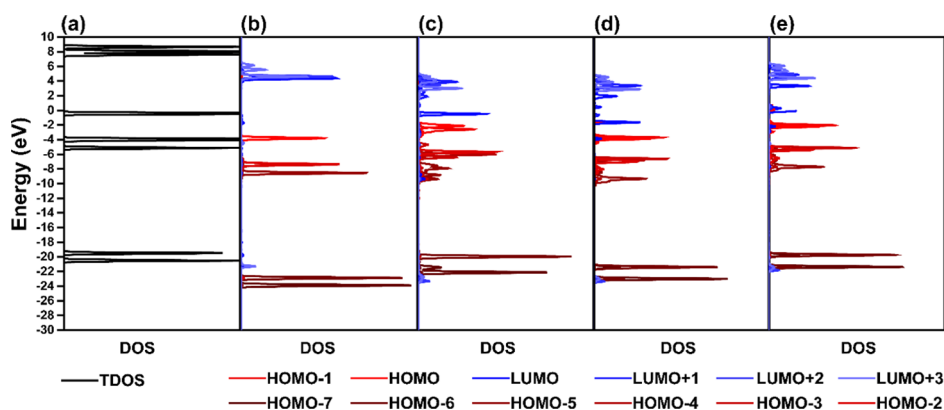
Figure 7. (a) Total DOS of free CO_2 molecule and MOPDOS of CO_2 adsorbed on (b) NPT-0, (c) NPT-Sn, (d) NPT-Co, and (e) NPT-Ni. Fermi energy level was set to 0 eV.
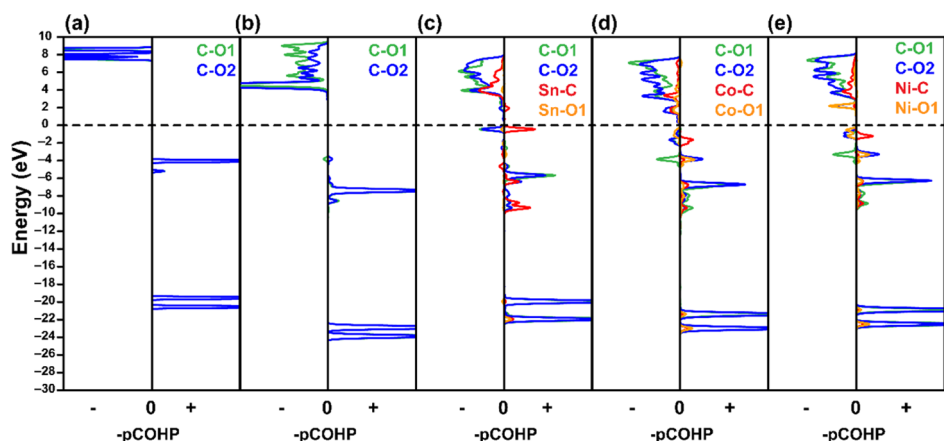
Figure 8. Crystal orbital Hamilton population (COHP) of (a) free CO_2 molecule, CO_2 adsorbed on (b) NPT-0, (c) NPT-Sn, (d) NPT-Co, and (e) NPT-Ni. Fermi energy level was set to 0 eV. Negative value represents antibonding states, and a positive value represents bonding states.

between metal atoms and nitrogen atoms increased and the corresponding ICOBI values decreased, suggesting a weaker covalent interaction between nitrogen atoms and metal atoms.

The C−O bonding strengths of CO_2 before and after adsorption are evaluated through ICOHP, ICOBI, and bond distances.[11,77,80−84] The ICOHP, ICOBI, and C−O distances in CO_2 were almost unchanged upon adsorption on NPT-0, indicating similar C−O bond strengths to free CO_2. Upon adsorption on metal-doped NPT, the C−O distances increased from 1.18 Å to around 1.2−1.3 Å and the ICOHP values increased, suggesting a weaker bond strength in adsorbed CO_2.

Charge density difference and Bader charge transfer analysis reveal that the Sn atom donates more electrons to the CO_2 molecule compared to Co and Ni atoms. However, the adsorption energy of CO_2 on NPT-Sn is weaker than that on NPT-Ni and NPT-Co. The significant charge transfer from Sn to CO_2 (Δq = 0.85 e) indicates a strong binding between CO_2 and Sn atoms, but the weaker binding of Sn to the NPT network (Table 1) resulted in a weaker overall CO_2 adsorption on NPT-Sn than in NPT-Co and NPT-Ni (Table 3).

CONCLUSIONS

In summary, our research found that adding small amounts of Co, Ni, or Sn to a polytriazine network improves its ability to adsorb CO_2. The presence of these metal atoms also significantly affects the electronic structure and HOMO−LUMO gap of the NPT structure. CO_2 is primarily chemisorbed on the metal-

Table 3. CO_2 Adsorption Energies (E_{ads}), Charge Transfers (Δq) Based on the Bader Charge Analysis, and Work Function Changes ($\Delta\phi$) of the Systems

CO_2 molecule in the system	CO_2-NPT-0	CO_2-NPT-Sn	CO_2-NPT-Ni	CO_2-NPT-Co
E_{ad} (eV)	−0.26	−0.69	−1.90	−1.76
Δq (e)[a]	−0.05	+0.85	+0.33	+0.45
$\Delta\phi$ (eV)[b]	+0.00	+1.27	+0.69	+0.64

[a]The positive (negative) sign of Δq indicates that the gas molecule accepts (donates) electrons. [b]The positive (negative) sign of $\Delta\phi$ indicates that the work function increases (decreases) upon CO_2 adsorption.

doped NPT structures, whereas it is mainly physisorbed on the pristine NPT. Among the three doped metal systems studied, the CO_2 adsorption capacity is the highest for NPT-Ni and NPT-Co and the lowest for NPT-Sn. These results suggest that metal-doped NPT has the potential to be an effective CO_2 capture material and that the incorporation of these metal atoms could enhance the performance of other organic frameworks as well. Overall, this study provides valuable insights into the use of metal-doped NPT for CO_2 capture and provides promising directions for future research in this field.

■ ASSOCIATED CONTENT

Ⓢ Supporting Information

The Supporting Information is available free of charge at https://pubs.acs.org/doi/10.1021/acsomega.3c00395.

> Different adsorption sites for metal atoms and CO_2 on NPT structure, local PDOSs of metal atom-doped NPT systems, total density of states for an isolated linear CO_2 molecule, adsorption geometry of CO_2 on NPT structures, PDOS of metal doping and MOPDOS of isolated CO_2 molecule, corresponding vibration mode of CO_2, and tables of calculated results (PDF)

■ AUTHOR INFORMATION

Corresponding Authors

Young Soo Kang − *Department of Environmental and Climate Technology, Korea Institute of Energy Technology, Naju-si, Jeollanam do 58217, Republic of Korea;* ⓘ orcid.org/0000-0001-5746-8171; Email: yskang@kentech.ac.kr

Kang Min Ok − *Department of Chemistry, Sogang University, Seoul 04107, Republic of Korea;* ⓘ orcid.org/0000-0002-7195-9089; Email: kmok@sogang.ac.kr

Authors

Hieu Minh Ngo − *Department of Chemistry, Sogang University, Seoul 04107, Republic of Korea;* ⓘ orcid.org/0000-0003-0029-0071

Umapada Pal − *Institute of Physics, Autonomous University of Puebla, Puebla, Pue 72570, Mexico;* ⓘ orcid.org/0000-0002-5665-106X

Complete contact information is available at:
https://pubs.acs.org/10.1021/acsomega.3c00395

Author Contributions

H.M.N. designed and conducted the computations, analyzed data, and drafted the manuscript and figures. H.M.N. and K.M.O. wrote, revised, and edited the manuscript. U.P. contributed to idealization of the work and revision of the manuscript. K.M.O. and Y.S.K. supervised the project. All authors approved the final version of the manuscript.

Notes

The authors declare no competing financial interest.

■ ACKNOWLEDGMENTS

■ REFERENCES

(1) Richter, B. *Beyond Smoke and Mirrors*; Cambridge University Press, 2010.

(2) Boot-Handford, M. E.; Abanades, J. C.; Anthony, E. J.; Blunt, M. J.; Brandani, S.; Mac Dowell, N.; Fernández, J. R.; Ferrari, M.-C.; Gross, R.; Hallett, J. P.; et al. Carbon capture and storage update. *Energy Environ. Sci.* **2014**, 7, 130−189.

(3) Chu, S.; Cui, Y.; Liu, N. The path towards sustainable energy. *Nat. Mater.* **2016**, 16, 16−22.

(4) Banerjee, R.; Phan, A.; Wang, B.; Knobler, C.; Furukawa, H.; O'Keeffe, M.; Yaghi, O. M. High-throughput synthesis of zeolitic imidazolate frameworks and application to CO_2 capture. *Science* **2008**, 319, 939−943.

(5) Hu, Z.; Wang, Y.; Shah, B. B.; Zhao, D. CO_2 Capture in Metal-Organic Framework Adsorbents: An Engineering Perspective. *Adv. Sustain. Syst.* **2019**, 3, 1800080.

(6) Chen, C.; Kim, J.; Ahn, W.-S. CO_2 capture by amine-functionalized nanoporous materials: A review. *Korean J. Chem. Eng.* **2014**, 31, 1919−1934.

(7) Creamer, A. E.; Gao, B. Carbon-Based Adsorbents for Postcombustion CO_2 Capture: A Critical Review. *Environ. Sci. Technol.* **2016**, 50, 7276−7289.

(8) Bamonte, S.; Shubhashish, S.; Khanna, H.; Shuster, S.; Rubio, S. J. B.; Suib, S. L.; Alpay, S. P.; Sahoo, S. Magnetically Doped Molybdenum Disulfide Layers for Enhanced Carbon Dioxide Capture. *ACS Appl. Mater. Interfaces* **2022**, 14, 27799−27813.

(9) Xu, S.; Wei, S.; Wang, L.; Liu, S.; Wang, M.; Liu, S.; Wang, Z.; Yang, T.; Lu, X. Li-decorated β1-graphyne for high-performance CO_2 capture and separation over N_2. *Appl. Surf. Sci.* **2022**, 605, 154724.

(10) Yoon, M.; Moon, D. New Zr (IV) based metal-organic framework comprising a sulfur-containing ligand: Enhancement of CO_2 and H_2 storage capacity. *Micropor. Mesopor. Mat.* **2015**, 215, 116−122.

(11) Ta, L. T.; Hamada, I.; Morikawa, Y.; Dinh, V. A. Adsorption of toxic gases on borophene: surface deformation links to chemisorptions. *RSC Adv.* **2021**, 11, 18279−18287.

(12) Talapaneni, S. N.; Singh, G.; Kim, I. Y.; AlBahily, K.; Al-Muhtaseb, A. H.; Karakoti, A. S.; Tavakkoli, E.; Vinu, A. Nanostructured Carbon Nitrides for CO_2 Capture and Conversion. *Adv. Mater.* **2020**, 32, No. e1904635.

(13) Jelmy, E. J.; Thomas, N.; Mathew, D. T.; Louis, J.; Padmanabhan, N. T.; Kumaravel, V.; John, H.; Pillai, S. C. Impact of structure, doping and defect-engineering in 2D materials on CO_2 capture and conversion. *React. Chem. Eng.* **2021**, 6, 1701−1738.

(14) Mishra, A. K.; Ramaprabhu, S. Nanostructured polyaniline decorated graphene sheets for reversible CO_2 capture. *J. Mater. Chem.* **2012**, 22, 3708−3712.

(15) Wahab, M. A.; Na, J.; Masud, M. K.; Hossain, M. S. A.; Alothman, A. A.; Abdala, A. Nanoporous carbon nitride with a high content of inbuilt N site for the CO_2 capture. *J. Hazard. Mater.* **2021**, 408, 124843.

(16) Yang, H.; He, C.; Fu, L.; Huo, J.; Zhao, C.; Li, X.; Song, Y. Capture and separation of CO_2 on BC_3 nanosheets: A DFT study. *Chin. Chem. Lett.* **2021**, 32, 3202−3206.

(17) Darvishnejad, M. H.; Reisi-Vanani, A. DFT-D3 calculations of the charge-modulated CO_2 capture of N/Sc-embedded graphyne: Compilation of some factors. *J. CO_2 Util.* **2021**, 46, 101469.

(18) Wang, C.; Fang, Y.; Duan, H.; Liang, G.; Li, W.; Chen, D.; Long, M. DFT study of CO_2 adsorption properties on pristine, vacancy and doped graphenes. *Solid State Commun.* **2021**, 337, 114436.

(19) Chaudhary, M.; Nayak, A. K.; Muhammad, R.; Pradhan, D.; Mohanty, P. Nitrogen-Enriched Nanoporous Polytriazine for High-Performance Supercapacitor Application. *ACS Sustain. Chem. Eng.* **2018**, 6, 5895−5902.

(20) Adio, S. O.; Ganiyu, S. A.; Usman, M.; Abdulazeez, I.; Alhooshani, K. Facile and efficient nitrogen modified porous carbon derived from sugarcane bagasse for CO_2 capture: Experimental and DFT investigation of nitrogen atoms on carbon frameworks. *Chem. Eng. J.* **2020**, 382, 122964.

(21) Lakhi, K. S.; Park, D.-H.; Singh, G.; Talapaneni, S. N.; Ravon, U.; Al-Bahily, K.; Vinu, A. Energy efficient synthesis of highly ordered mesoporous carbon nitrides with uniform rods and their superior CO_2 adsorption capacity. *J. Mater. Chem. A* **2017**, 5, 16220−16230.

(22) Park, D. H.; Lakhi, K. S.; Ramadass, K.; Kim, M. K.; Talapaneni, S. N.; Joseph, S.; Ravon, U.; Al-Bahily, K.; Vinu, A. Energy Efficient Synthesis of Ordered Mesoporous Carbon Nitrides with a High

Nitrogen Content and Enhanced CO_2 Capture Capacity. *Chemistry* **2017**, *23*, 10753−10757.

(23) Zhang, H.-p.; Du, A.; Gandhi, N. S.; Jiao, Y.; Zhang, Y.; Lin, X.; Lu, X.; Tang, Y. Metal-doped graphitic carbon nitride (g-C_3N_4) as selective NO_2 sensors: A first-principles study. *Appl. Surf. Sci.* **2018**, *455*, 1116−1122.

(24) Bae, J.; Lee, C. Y.; Jeong, N. C. Weak Coordination Bond of Chloromethane: A Unique Way to Activate Metal Node Within an Unstable Metal−Organic Framework DUT-34. *Bull. Korean Chem. Soc.* **2021**, *42*, 658−666.

(25) Hu, F.; Tong, S.; Lu, K.; Chen, C.-M.; Su, F.-Y.; Zhou, J.; Lu, Z.-H.; Wang, X.; Feng, G.; Zhang, R. Reduced graphene oxide supported Ni-Ce catalysts for CO_2 methanation: The support and ceria promotion effects. *J. CO_2 Util.* **2019**, *34*, 676−687.

(26) Jin, C.; Cheng, L.; Feng, G.; Ye, R.; Lu, Z. H.; Zhang, R.; Yu, X. Adsorption of Transition-Metal Clusters on Graphene and N-Doped Graphene: A DFT Study. *Langmuir* **2022**, *38*, 3694−3710.

(27) Shee, N. K.; Lee, C. J.; Kim, H. J. Hexacoordinated Sn(IV) porphyrin-based square-grid frameworks exhibiting selective uptake of CO_2 over N_2. *Bull. Korean Chem. Soc.* **2021**, *43*, 103−109.

(28) Homlamai, K.; Maihom, T.; Choomwattana, S.; Sawangphruk, M.; Limtrakul, J. Single-atoms supported (Fe, Co, Ni, Cu) on graphitic carbon nitride for CO_2 adsorption and hydrogenation to formic acid: First-principles insights. *Appl. Surf. Sci.* **2020**, *499*, 143928.

(29) Chen, J.; Fang, S.; Shen, Q.; Fan, J.; Li, Q.; Lv, K. Recent Advances of Doping and Surface Modifying Carbon Nitride with Characterization Techniques. *Catalysts* **2022**, *12*, 962.

(30) Fao, G. D.; Jiang, J.-C. Theoretical investigation of CO_2 conversion on corrugated g-C_3N_4 Surface decorated by single-atom of Fe, Co, and Pd. *Mol. Catal.* **2022**, *526*, 112402.

(31) Peng, R.; Gao, Y.; Younus, H. A.; Zhang, Y.; Ni, W.; Zhang, S. Electrochemical CO2-to-Formate Conversion Over Positive Charge Depleted Tin Sites. *ACS Appl. Energy Mater.* **2022**, *5*, 9324−9332.

(32) Cao, Z.; Liu, S.; Xu, K.; Mao, Y.; Wu, Y.; Mao, Q. Predictable interfacial mass transfer intensification of Sn−N doped multichannel hollow carbon nanofibers for the CO_2 electro-reduction reaction. *Sustain. Energy Fuels* **2021**, *5*, 3097−3101.

(33) Syzgantseva, M. A.; Ireland, C. P.; Ebrahim, F. M.; Smit, B.; Syzgantseva, O. A. Metal Substitution as the Method of Modifying Electronic Structure of Metal-Organic Frameworks. *J. Am. Chem. Soc.* **2019**, *141*, 6271−6278.

(34) Dai, R.; Sun, W.; Wang, Y. Ultrasmall Tin Nanodots Embedded in Nitrogen-Doped Mesoporous Carbon: Metal-Organic-Framework Derivation and Electrochemical Application as Highly Stable Anode for Lithium Ion Batteries. *Electrochim. Acta* **2016**, *217*, 123−131.

(35) Blöchl, P. E. Projector augmented-wave method. *Phys. Rev. B. Condens. Matter.* **1994**, *50*, 17953−17979.

(36) Hohenberg, P.; Kohn, W. Inhomogeneous Electron Gas. *Phys. Rev.* **1964**, *136*, B864−B871.

(37) Kohn, W.; Sham, L. J. Self-Consistent Equations Including Exchange and Correlation Effects. *Phys. Rev.* **1965**, *140*, A1133−A1138.

(38) Kresse, G.; Furthmüller, J. Efficient iterative schemes for ab initio total-energy calculations using a plane-wave basis set. *Phys. Rev. B. Condens. Matter.* **1996**, *54*, 11169−11186.

(39) Kresse, G.; Joubert, D. From ultrasoft pseudopotentials to the projector augmented-wave method. *Phys. Rev. B* **1999**, *59*, 1758−1775.

(40) Perdew, J. P.; Burke, K.; Ernzerhof, M. Generalized Gradient Approximation Made Simple. *Phys. Rev. Lett.* **1996**, *77*, 3865−3868.

(41) Grimme, S.; Antony, J.; Ehrlich, S.; Krieg, H. A consistent and accurate ab initio parametrization of density functional dispersion correction (DFT-D) for the 94 elements H-Pu. *J. Chem. Phys.* **2010**, *132*, 154104.

(42) Wang, V.; Xu, N.; Liu, J.-C.; Tang, G.; Geng, W.-T. VASPKIT: A user-friendly interface facilitating high-throughput computing and analysis using VASP code. *Comput. Phys. Commun.* **2021**, *267*, 108033.

(43) Momma, K.; Izumi, F. VESTA 3 for three-dimensional visualization of crystal, volumetric and morphology data. *J. Appl. Crystallogr.* **2011**, *44*, 1272−1276.

(44) Kitchin, J. R. *Modeling materials using density functional theory*; Self-published, 2012.

(45) Rivera-Cárcamo, C.; Serp, P. Single Atom Catalysts on Carbon-Based Materials. *ChemCatChem* **2018**, *10*, 5058−5091.

(46) O'Connor, N. J.; Jonayat, A. S. M.; Janik, M. J.; Senftle, T. P. Interaction trends between single metal atoms and oxide supports identified with density functional theory and statistical learning. *Nat. Cat.* **2018**, *1*, 531−539.

(47) Du, J.; Xia, C.; Xiong, W.; Zhao, X.; Wang, T.; Jia, Y. Tuning the electronic structures and magnetism of two-dimensional porous C_2N via transition metal embedding. *Phys. Chem. Chem. Phys.* **2016**, *18*, 22678−22686.

(48) Figueroba, A.; Kovács, G.; Bruix, A.; Neyman, K. M. Towards stable single-atom catalysts: strong binding of atomically dispersed transition metals on the surface of nanostructured ceria. *Catal. Sci. Technol.* **2016**, *6*, 6806−6813.

(49) Putra, S. E. M.; Morikawa, Y.; Hamada, I. Isotope effect of methane adsorbed on fcc metal (1 1 1) surfaces. *Chem. Phys. Lett.* **2021**, *2021*, 780.

(50) Tang, W.; Sanville, E.; Henkelman, G. A grid-based Bader analysis algorithm without lattice bias. *J. Phys. Condens. Mat.* **2009**, *21*, 084204.

(51) Lüftner, D.; Weiß, S.; Yang, X.; Hurdax, P.; Feyer, V.; Gottwald, A.; Koller, G.; Soubatch, S.; Puschnig, P.; Ramsey, M. G.; et al. Understanding the photoemission distribution of strongly interacting two-dimensional overlayers. *Phys. Rev. B* **2017**, *96*, 125402.

(52) Nelson, R.; Ertural, C.; George, J.; Deringer, V. L.; Hautier, G.; Dronskowski, R. LOBSTER: Local orbital projections, atomic charges, and chemical-bonding analysis from projector-augmented-wave-based density-functional theory. *J. Comput. Chem.* **2020**, *41*, 1931−1940.

(53) Müller, P. C.; Ertural, C.; Hempelmann, J.; Dronskowski, R. Crystal Orbital Bond Index: Covalent Bond Orders in Solids. *J. Phys.Chem. C* **2021**, *125*, 7959−7970.

(54) George, J.; Petretto, G.; Naik, A.; Esters, M.; Jackson, A. J.; Nelson, R.; Dronskowski, R.; Rignanese, G. M.; Hautier, G. Automated Bonding Analysis with Crystal Orbital Hamilton Populations. *ChemPlusChem* **2022**, *87*, No. e202200123.

(55) Ong, S. P.; Richards, W. D.; Jain, A.; Hautier, G.; Kocher, M.; Cholia, S.; Gunter, D.; Chevrier, V. L.; Persson, K. A.; Ceder, G. Python Materials Genomics (pymatgen): A robust, open-source python library for materials analysis. *Comp. Mater. Sci.* **2013**, *68*, 314−319.

(56) Waroquiers, D.; George, J.; Horton, M.; Schenk, S.; Persson, K. A.; Rignanese, G. M.; Gonze, X.; Hautier, G. ChemEnv: a fast and robust coordination environment identification tool. *Acta. Crystallogr. B. Struct. Sci. Cryst. Eng. Mater.* **2020**, *76*, 683−695.

(57) Maintz, S.; Deringer, V. L.; Tchougréeff, A. L.; Dronskowski, R. Analytic projection from plane-wave and PAW wavefunctions and application to chemical-bonding analysis in solids. *J. Comput. Chem.* **2013**, *34*, 2557−2567.

(58) Maintz, S.; Deringer, V. L.; Tchougréeff, A. L.; Dronskowski, R. LOBSTER: A tool to extract chemical bonding from plane-wave based DFT. *J. Comput. Chem.* **2016**, *37*, 1030−1035.

(59) *wxDragon program*; RWTH Aachen University: Aachen: Deutschland, 2016.

(60) Bloch, F. Über die Quantenmechanik der Elektronen in Kristallgittern. *Z. Phys.* **1929**, *52*, 555−600.

(61) Wirnhier, E.; Döblinger, M.; Gunzelmann, D.; Senker, J.; Lotsch, B. V.; Schnick, W. Poly(triazine imide) with intercalation of lithium and chloride ions $[(C_3N_3)_2(NH_xLi_{1-x})_3 \cdot LiCl]$: a crystalline 2D carbon nitride network. *Chemistry* **2011**, *17*, 3213−3221.

(62) Burmeister, D.; Tran, H. A.; Müller, J.; Guerrini, M.; Cocchi, C.; Plaickner, J.; Kochovski, Z.; List-Kratochvil, E. J. W.; Bojdys, M. J. Optimized Synthesis of Solution-Processable Crystalline Poly(Triazine Imide) with Minimized Defects for OLED Application. *Angew. Chem., Int. Ed.* **2022**, *61*, No. e202111749.

(63) Villalobos, L. F.; Vahdat, M. T.; Dakhchoune, M.; Nadizadeh, Z.; Mensi, M.; Oveisi, E.; Campi, D.; Marzari, N.; Agrawal, K. V. Large-scale synthesis of crystalline g-C_3N_4 nanosheets and high-temperature H_2 sieving from assembled films. *Sci. Adv.* **2020**, *6*, No. eaay9851.

(64) Mesch, M. B.; Bärwinkel, K.; Krysiak, Y.; Martineau, C.; Taulelle, F.; Neder, R. B.; Kolb, U.; Senker, J. Solving the Hydrogen and Lithium Substructure of Poly(triazine imide)/LiCl Using NMR Crystallography. *Chemistry* **2016**, *22*, 16878−16890.

(65) Bhunia, M. K.; Melissen, S.; Parida, M. R.; Sarawade, P.; Basset, J.-M.; Anjum, D. H.; Mohammed, O. F.; Sautet, P.; Le Bahers, T.; Takanabe, K. Dendritic Tip-on Polytriazine-Based Carbon Nitride Photocatalyst with High Hydrogen Evolution Activity. *Chem. Mater.* **2015**, *27*, 8237−8247.

(66) Chong, S. Y.; Jones, J. T. A.; Khimyak, Y. Z.; Cooper, A. I.; Thomas, A.; Antonietti, M.; Bojdys, M. J. Tuning of gallery heights in a crystalline 2D carbon nitride network. *J. Mater. Chem. A* **2013**, *1*, 1102−1107.

(67) Wang, Y.; Jia, X.; Li, L.; Yang, J.; Li, J. Selective adsorption of propene over propane on Li-decorated poly (triazine imide). *Green Energy Environ* **2022**, *7*, 307−313.

(68) Ball, B.; Chakravarty, C.; Sarkar, P. Two-Dimensional Covalent Triazine Framework as a Promising Anode Material for Li-Ion Batteries. *J. Phys.Chem. C* **2019**, *123*, 30155−30164.

(69) Yang, C.; Zhao, Z. Y.; Wei, H. T.; Deng, X. Y.; Liu, Q. J. DFT calculations for single-atom confinement effects of noble metals on monolayer g-C_3N_4 for photocatalytic applications. *RSC Adv.* **2021**, *11*, 4276−4285.

(70) Niu, H.; Zhang, Z.; Wang, X.; Wan, X.; Shao, C.; Guo, Y. Theoretical Insights into the Mechanism of Selective Nitrate-to-Ammonia Electroreduction on Single-Atom Catalysts. *Adv. Funct. Mater.* **2020**, *31*, 2008533.

(71) Ertural, C.; Steinberg, S.; Dronskowski, R. Development of a robust tool to extract Mulliken and Lowdin charges from plane waves and its application to solid-state materials. *RSC Adv.* **2019**, *9*, 29821−29830.

(72) Kittel, C. *Introduction to Solid State Physics*; Wiley, 2004.

(73) Wang, Y.; Meng, Z.; Liu, Y.; You, D.; Wu, K.; Lv, J.; Wang, X.; Deng, K.; Rao, D.; Lu, R. Lithium decoration of three dimensional boron-doped graphene frameworks for high-capacity hydrogen storage. *Appl. Phys. Lett.* **2015**, *106*, 063901.

(74) Hu, T.; Hong, J. First-Principles Study of Metal Adatom Adsorption on Black Phosphorene. *J. Phys.Chem. C* **2015**, *119*, 8199−8207.

(75) Ong, W. J.; Tan, L. L.; Ng, Y. H.; Yong, S. T.; Chai, S. P. Graphitic Carbon Nitride (g-C_3N_4)-Based Photocatalysts for Artificial Photosynthesis and Environmental Remediation: Are We a Step Closer To Achieving Sustainability? *Chem. Rev.* **2016**, *116*, 7159−7329.

(76) Bendavid, L. I.; Carter, E. A. CO_2 Adsorption on $Cu_2O(111)$: A DFT+U and DFT-D Study. *J. Phys.Chem. C* **2013**, *117*, 26048−26059.

(77) Hoffmann, R. *Solids and Surfaces: A Chemist's View of Bonding in Extended Structures*; Wiley-VCH, 1989.

(78) Gudmundsdóttir, S.; Tang, W.; Henkelman, G.; Jónsson, H.; Skúlason, E. Local density of states analysis using Bader decomposition for N_2 and CO_2 adsorbed on Pt(110)-(1 × 2) electrodes. *J. Chem. Phys.* **2012**, *137*, 164705.

(79) Dronskowski, R.; Bloechl, P. E. Crystal orbital Hamilton populations (COHP): energy-resolved visualization of chemical bonding in solids based on density-functional calculations. *J. Phys. Chem. B* **2002**, *97*, 8617−8624.

(80) Gu, H.; Liu, X.; Liu, X.; Ling, C.; Wei, K.; Zhan, G.; Guo, Y.; Zhang, L. Adjacent single-atom irons boosting molecular oxygen activation on MnO_2. *Nat. Commun.* **2021**, *12*, 5422.

(81) Liu, Y. Reduction Mechanism of NO Gas on Iron−Phthalocyanines (Fe−PCs): A DFT Investigation. *Catal. Lett.* **2021**, *152*, 1338−1346.

(82) Hoffmann, R. A chemical and theoretical approach to bonding at surfaces. *J. Phys. Condens. Mat.* **1993**, *5*, A1−A16.

(83) Hoffmann, R. A chemical and theoretical way to look at bonding on surfaces. *Rev. Mod. Phys.* **1988**, *60*, 601−628.

(84) Oana, M.; Hoffmann, R.; Abruña, H. D.; DiSalvo, F. J. Adsorption of CO on $PtBi_2$ and PtBi surfaces. *Surf. Sci.* **2005**, *574*, 1−16.